Acquisition of linograms in SPET: implementation and benefits

Stephan Walrand[1], Aad van Dulmen[2], Henk van Rossem[2], Stanislas Pauwels[1]

[1] Centre of Nuclear Medicine, Catholic University of Louvain, 54.30 Av Hippocrate, 1200 Brussels, Belgium
[2] Loodsman technology transfer i.o. 1871CZ Schoorl, the Netherlands

Received 11 February and in revised form 14 April 2002 / Published online: 18 June 2002

Abstract. Compared with other tomographic modalities, single-photon emission tomography (SPET), the most widely used tomographic modality in nuclear medicine, suffers from poor quality image since the collimator stops 99.99% of the emitted gamma rays reaching the detector. This paper describes a new SPET acquisition modality using a very short focal length (12.5 cm) fan-beam collimator and a very short transverse field of view detector (25 cm). The detector moves along at least two linear orthogonal orbits in such a way that the focal line travels through the source target. This linear orbit acquisition (LOrA) generates linograms forming a complete set of tomographic data, i.e. sufficient to exactly reconstruct the activity map using a modified filtered back-projection algorithm. In contrast to the classical fan-beam tomography, truncation is not a problem, even when the source transverse size is much larger than the detector transverse size. When the collimator hole length/diameter ratio is adapted to obtain a spatial resolution similar to that of classical SPET, LOrA SPET offers an improvement in sensitivity by a factor of about 2.5 for a 20-cm source size. This improvement is achieved with a detector that is half as large, and thus half as expensive. As with classical fan-beam SPET, the sensitivity increases further if the target size decreases. When fitting the collimator to obtain a similar sensitivity to that of classical SPET, a significant improvement in spatial resolution is obtained.

Keywords: SPET – Linogram – Fan-beam – Truncation

Eur J Nucl Med (2002) 29:1188–1197
DOI 10.1007/s00259-002-0862-x

Stephan Walrand (✉)
Centre of Nuclear Medicine,
Catholic University of Louvain,
54.30 Av Hippocrate, 1200 Brussels, Belgium
e-mail: walrand@mnuc.ucl.ac.be
Fax: +32-2-7645408

Introduction

The introduction of the tomographic technique in medicine (CT scan, MRI, SPET, PET) represented a great improvement in that it allowed the non-invasive study of regional morphology/metabolism. Compared with the other tomographic modalities, SPET suffers from poor image quality. The collimator stops about 99.99% of the gamma rays reaching the detector; this leads to a poor signal to noise ratio in conjunction with a poor spatial resolution [1]. Using parallel-hole collimators, modification of the hole length or hole diameter in order to improve one of these properties is always to the detriment of the other one.

In an attempt to improve the SPET sensitivity-resolution combination, the use of a fan-beam collimator was proposed [1, 2, 3, 4]: for the same hole feature, i.e. similar spatial resolution, the fan-beam collimator has a sensitivity which dramatically increases when approaching the focal line. However, when using the classical tomography technique, i.e. planar views acquired along a revolving orbit around the patient, the whole activity has to be included in the collimator acceptance area at each angle. Failure to do so causes the reconstructed images to be corrupted by significant truncation artefacts [1, 2]. This necessitates the use of dedicated fan-beam collimators with a long focal length: >40 cm for a brain study and >60 cm for a general study. In addition the set-up of the orbit map is very problematic. To avoid truncation, the target is generally set close to the collimator, where its characteristics are similar to those of the parallel collimator. As a consequence a large majority of nuclear medicine centres do not use fan-beam collimators in clinical routine.

In a previous publication [5] we proposed the use of a novel SPET modality called LOrA (linear orbit acquisition), which uses a short focal length fan-beam collimator (12.5 cm) for all organ studies without truncation and positioning problems, and furthermore with the possibility of setting the target organ on the focal line to increase the sensitivity. The data are no longer acquired along a revolving orbit around the patient, but along at least two orthogonal linear orbits, resulting in linogram acquisition rather than a classical sinogram. Edhlom and Herman originally proposed the use of linogram in tomography applications [6, 7]. They showed that linogram reconstruction has better computational features than sinogram reconstruction. They proposed the uses of linograms for PET reconstruction with a linear array of detectors and also an X-ray transmission scanner device, directly providing linogram acquisition. The goal of the present paper is to show that acquiring linograms in SPET improves the performance of the device acquisition as well.

Surprisingly, the first tomographic device, which was proposed by Anger in 1966 [8], partially offered these features. Nevertheless, this system, called longitudinal tomography, used a rectilinear scanner equipped with a cone-beam collimator, with movement along one orbit perpendicular to the transverse plane. This modality did not allow reconstruction of the activity by replacing the detected events to their emission positions, as does SPET. It only generated images by adding events in such a way that all activities outside of a selected plane appeared blurred. Even though some algorithms [9, 10] were developed to enhance the contrast, they removed only a part of the blurred out of focus background and acted only in limited angle reconstructions, explaining why the SPET rotating camera superseded this method in the 1980s.

Materials and methods

Acquisition and reconstruction of linograms in SPET. Using the classical revolving orbit, different sources included in the collimator acceptance area at each angle ϕ lead to different complete (r, ϕ) trajectories (top row, Fig. 1). Knowing these trajectories, called sinograms, one can reconstruct the activity distribution, using the well-known filtered back-projection (FBP) algorithm for example [11]. When the sources are not always in the acceptance collimator area, the (r, ϕ) trajectories are not complete (bottom row, Fig. 1). Furthermore, when rotating around the focal line, two sources placed in opposition versus the focal line project their activities at the same crystal position and, thus, have similar (r, ϕ) trajectories. In other words, when some activity leaves the collimator acceptance area during the revolution, or when the rotation axis approaches the focal line, the uncertainties increase, and the activity distribution can no longer be reconstructed [1, 2].

When the relative collimator-source rotation ϕ is replaced by a relative linear shift V, the (r, V) trajectories are always different and complete for sources located anywhere in front of the collimator (Fig. 2). These trajectories are called linograms and are known to give better tomographic reconstruction [6, 7], offering replacement of computational expensive back-projection by a series of fast Fourier transforms and potential improvement in accuracy by avoidance of interpolation during the reconstruction process.

The straight line integral (Fig. 3) giving the measured activity P_α (U_α, V, r) from an activity distribution $A(x, y)$, with the collimator perpendicular to the α axis (α=x or α=y), is:

$$\begin{aligned} P_x(U_x,V,r) &= f\int_{-\infty}^{+\infty} A(-U_x+\lambda f, V-\lambda r)\,d\lambda \\ P_y(U_y,V,r) &= f\int_{-\infty}^{+\infty} A(V-\lambda r, -U_y+\lambda f)\,d\lambda \end{aligned} \quad (1)$$

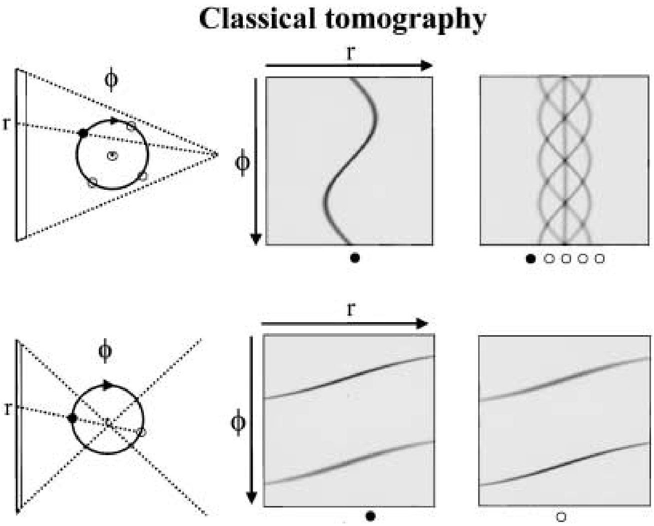

Fig. 1. Sinograms obtained for point sources using a fan-beam collimator in classical rotating tomography. r, Crystal transverse coordinate; ϕ, rotation angle; rotation orbits are represented in the camera reference system

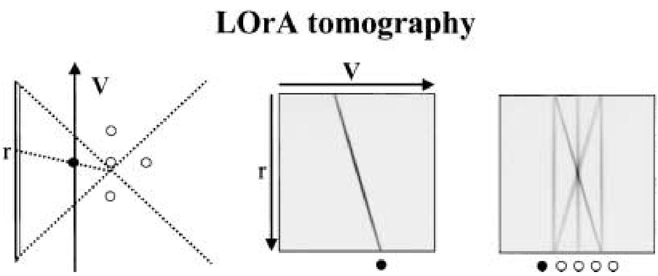

Fig. 2. Linograms obtained for point sources using a fan-beam collimator moving along a linear orbit acquisition (LOrA). r, Crystal transverse coordinate; V, linear shift; the linear orbit is represented in the camera reference system

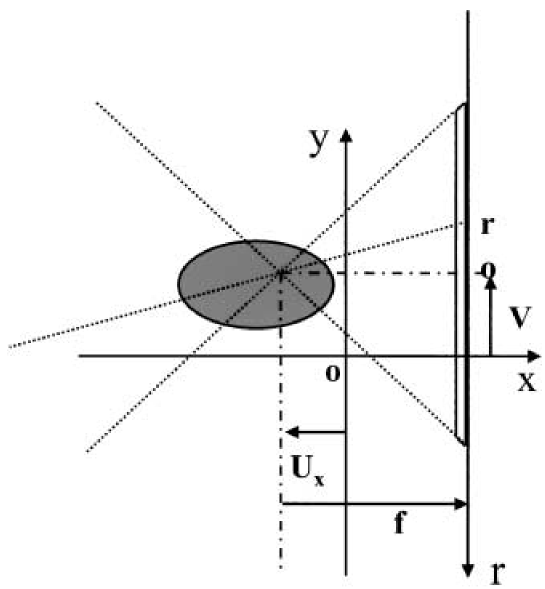

Fig. 3. Acquisition geometry for the projection P_x

where λ is the coordinate along the projection line and f is the fan-beam collimator focal length. The orbit coordinate V is the focal line shift from the coordinate axis perpendicular to the collimator (axis x for P_x and axis y for P_y). U_α is the focal line shift from the coordinate axis parallel to the collimator (axis y for P_x and axis x for P_y). U_α is constant along the linear orbit. r is the transverse coordinate on the detector area.

Using Fourier transforms (see Appendix A), an FBP relation is obtained which can be used to reconstruct the activity distribution (throughout the paper, uppercase refers to the function in the real space, and lowercase to the Fourier transform of the function):

$$A(x,y) = \frac{1}{(2\pi)^2 f}\int_{-f}^{+f}\left(\tilde{P}_x\left(\frac{r}{f}x+y,r\right) + \tilde{P}_y\left(x+\frac{r}{f}y,r\right)\right)dr \quad (2)$$

with:

$$\tilde{p}_\alpha(k,r) = |k|\, p_\alpha(U_\alpha,k,r)\, e^{ikU_\alpha \frac{r}{f}} \quad (3)$$

where α=x or α=y, and k is the spatial frequency of the linear orbit. Thus the activity distribution A is completely known in the Fourier space using two orthogonal linear orbits if the transverse detector field of view (FOV) is greater than two times the collimator focal length, independently of the target transverse size, i.e.:

$r \in [-f, f]$

Equation 3 is the ramp filtered linogram. It is to be noted – and it is the key difference from classical SPET – that the orbit coordinate V (or r) in LOrA plays the role of the detector transverse coordinate r (or ϕ) in classical SPET. As a consequence, LOrA SPET should be affected by the detector uniformity in a different way to classical SPET.

Due to the gamma attenuation, it would be advantageous to perform the two orthogonal linear orbits along the body side closest to the target organ, or to perform four linear orbits forming a rectangle when the target is the whole body slice.

Numerical simulations. Two phantoms were simulated:

- A 256×256 pixel map (pixel size 1.5625 mm) of the Jaszczak de luxe phantom. The numerical simulated projections of the phantom map were computed in a 128×128 matrix (3.125 mm pixel size) along the four linear orbits. No attenuation was introduced.
- A 128×128 pixel map (pixel size 4.4 mm) simulating a cardiac study. The liver activity was 50% of the heart activity. An effective attenuation (μ=0.11cm^{-1}) was assumed inside an elliptical contour (44×30 cm). Only the two linear orbits closest to the heart were used (upper side and left side). The sampling was 128 bins along the transverse detector coordinate (size 3.125 mm), and the step width was 4.4 mm along the linear orbits. The phantom was reconstructed with the whole orbit length and with the portions of the orbits corresponding to the heart area.

A shift of the focal versus the axis origin (U_α) is used to fix the distance from the phantom to the collimator. The collimators were simulated by an infinitely attenuating plate (no septal penetration and null thickness) perforated with square holes. The projections were computed in two dimensions, with the same sensitivity in the longitudinal direction for both modalities. The crystal PSF was simulated by a gaussian function of 3.5 mm full-width at half-maximum (FWHM). Gamma scattering in the phantom medium and in the collimator was neglected. No noise was added to the tomographic projections. The reconstructions were performed in a 256×256 dimension matrix using the classical FBP algorithm [11] for parallel collimator classical SPET, and using the classical FBP algorithm [11] after spatial sinogram rebinning [4] for fan-beam collimator classical SPET. The goal being to compare the acquisition device performances, the FBP algorithm (Eqs. 2, 3) was used for LOrA SPET rather than the more powerful and more accurate method proposed by Edhlom et al. [6, 7]. The final reconstruction was the summation of the FBP reconstruction of the four couples of adjacent orthogonal orbits. No noise filter or spatial resolution recovery filter was used. The hole length (40 mm) and hole diameter (1.8 mm) used in the classical SPET simulations correspond to a low-energy high-resolution (LEHR) collimator, the most widely used in SPET. All simulations were performed in one transverse slice: source distribution, acquired projection, and reconstructed slice. Simulations with various acquisition pixel sizes and with a uniformity defect were performed.

Fig. 4. Acquisition set-up. *A*, Fan-beam collimator inserted in the lead shielding; *B*, parallel-hole collimator; *C*, linear positioning system; *D*, Jaszczak phantom fixed on a rotating plate

Phantom acquisitions. A one-slice (4 mm width) fan-beam collimator with a short focal length (f=13 cm) was built. It was composed of two copper plates (28×3×0.5 cm) separated by 4 mm. Straight grooves (0.4 mm width, 0.75 mm depth) pointing to the focal point were made in the two plate sides (28×3cm) facing each other along a length of 24 cm (the digital tool did not allow production of grooves sufficiently slanted to cover the whole collimator length). The distance between the groove centres was 1.9 mm along the plate side facing the focal point. Lead sheets (0.3 mm thickness, 5 mm width) were slipped between the two plates along the grooves. This was the most difficult step in the building process: avoiding some small ripples on the lead sheets was a tricky job. The useful field of view of the collimator was 24×0.4 cm. In order to compare classical SPET under similar conditions, a parallel collimator was built in the same way, with a distance between the groove centres of 1.7 mm. The acquisitions were performed using a GE 400 AC camera (General Electric, Milwaukee, USA), the collimators being inserted in a lead plate (1 cm thickness) fixed on the detector (Fig. 4).

In order to avoid use of extremely high activity, a Jaszczak de luxe phantom reduced to 1.2 cm longitudinal length was built. For the LOrA acquisition the phantom was screwed on a rotating plate held by a linear positioning system (500KBS100, Fohrenbach GmbH). A stepper motor (4H56-9 L0602-A, Nanotec Electronic GmbH) controlled by a PC plug-in card (SM30, Owis, Staufen

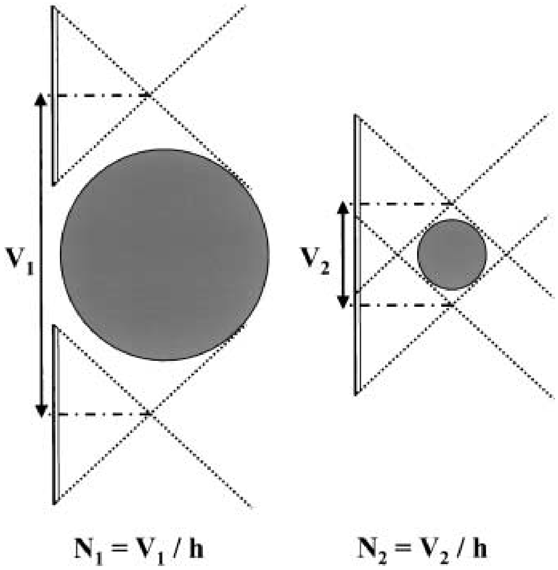

Fig. 5. Orbit range needed for LOrA SPET. V_i, Non-null count orbit range; N_i, sampling number needed in the linear orbit; h, pixel size of the reconstruction

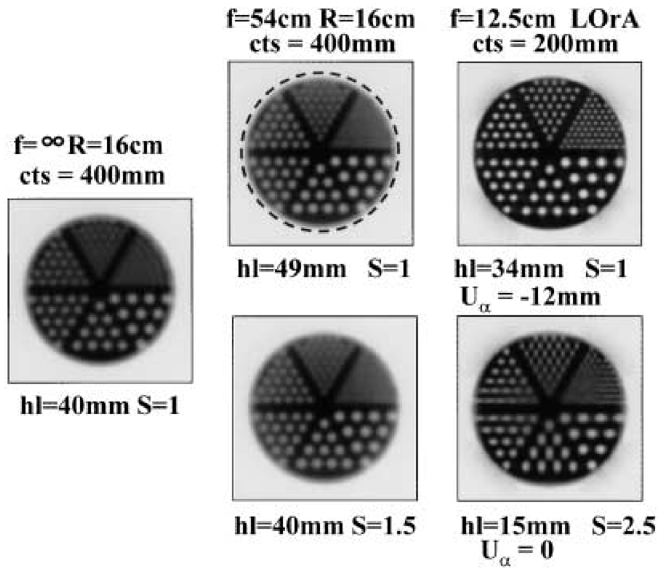

Fig. 6. Comparison of transverse slices obtained for the Jaszczak de luxe phantom by numerical simulation for parallel classical SPET (*left column*), fan-beam classical SPET (*middle column*) and LOrA SPET (*right column*). *R*, classical rotation radius length measured from the detector surface; *hl*, collimator hole length (hole transverse width is 1.8 mm for all collimators), *f*, fan-beam collimator focal length measured from the detector surface; *S*, relative sensitivity, cts, crystal transverse size (FOV). The *dotted circle* (*middle column*) represents the FOV of the classical fan-beam SPET. *Top row: hl* fitted to obtain similar sensitivity. *Bottom row: hl* fitted to obtain similar spatial resolution to classical parallel SPET. U_α is used to fix the distance between the collimator and the phantom edge

GmbH) was used to draw the positioning system. The phantom was turned by hand to perform the four linear orbits (0º, 90º, 180º, 270º). The positioning table was set up in relation to the camera using a rule.

Three acquisitions were performed for each modality: 120, 7.5 and 7.5 min total acquisition time with the phantom filled respectively with 481, 481 and 37 MBq of technetium-99m. For LOrA, 74 planar views (128×128 matrix, 3.125 mm pixel size) were acquired along the four linear orbits (23.125 cm total length, 3.125 mm linear step). For classical tomography, 128 planar views (128×128 matrix, 3.125 mm pixel size) were acquired along the 360º of the circular orbit (2.8125º angular step). For both modalities the distance between the phantom and the collimator was 1 cm.

A uniform source acquisition (cobalt-57) was used to correct the classical tomography acquisition for the uniformity defects of the camera and of the collimator as well. No uniformity correction was applied for the LOrA acquisition.

A noise-free numerical simulation was performed for both modalities taking into account a constant attenuation (0.11 cm^{-1}) inside the phantom, but neglecting the Compton scattering. Numerical simulation of Compton scattering requires advanced expertise in Monte Carlo computation.

The data were reconstructed in a 128×128 matrix (6.25 mm pixel size) in the same way as for the numerical simulations, i.e. using an FBP algorithm with no noise filtering and no spatial resolution recovery.

Results

Benefit of acquiring linograms in SPET

One immediate benefit of LOrA SPET is the absence of any truncation problems, even when the target size is greater than the camera FOV; this is especially relevant in SPET, given the difficulties in building large FOV gamma detectors. Indeed, for the computation of the ramp filtered linogram (Eqs. 2, 3), Eq. 1 shows that the orbit range has only to be adapted to the target transverse size. Thus the target of interest can easily be positioned in front of the collimator, the linear orbit length being fitted to the target size (Fig. 5). As a consequence the LOrA SPET sensitivity increases linearly as the target size decreases, improving the signal to noise ratio. Indeed, the number of projections needed to reconstruct the activity distribution is about the target size divided by the reconstruction pixel size *h*.

Numerical simulations

Numerical simulations for the Jaszczak de luxe phantom clearly showed, for a similar sensitivity, a significant improvement in spatial resolution with the LOrA SPET system in comparison with parallel or even fan-beam classical tomography: the contrast was higher for all the sectors (top row, Fig. 6). Furthermore, with classical fan-beam tomography the target size was limited (dotted circle, Fig. 6). LOrA SPET showed a light diagonal arte-

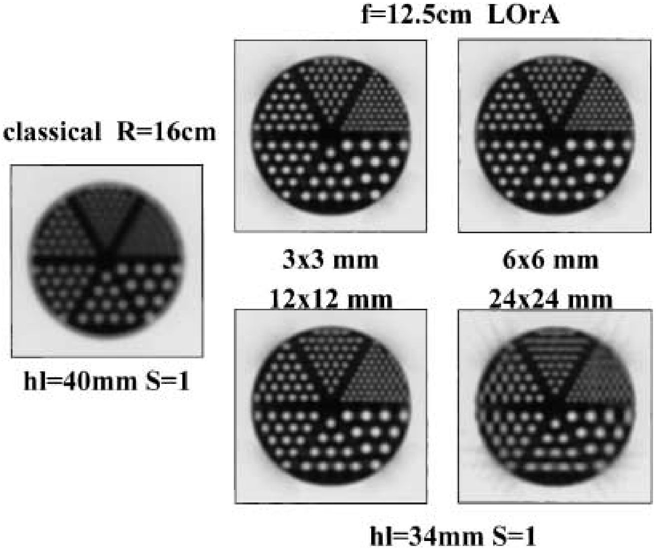

Fig. 7. Comparison of transverse slices obtained by numerical simulation for parallel classical SPET (*left*) and LOrA SPET (*right*) using various projection pixel sizes. Symbols as defined in the legend to Fig. 6

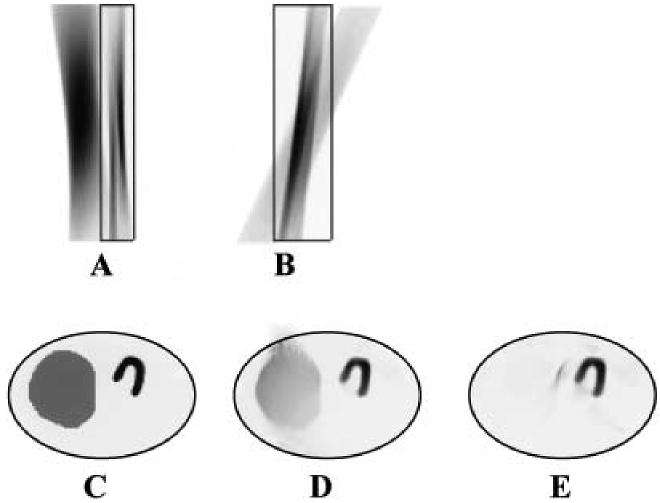

Fig. 9A–E. Simulation of a cardiac study using LOrA SPET with two orthogonal linear orbits. **A, B** Linogram corresponding to the upper and left orbit. **C** True activity. **D** Reconstruction of the whole orbits. **E** Reconstruction of the orbit range corresponding to the heart area (*black rectangles* in **A** and **B**). Hole length =34 mm, hole transverse width =1.8 mm, focal length =12.5 cm, attenuation =0.11 cm^{-1}

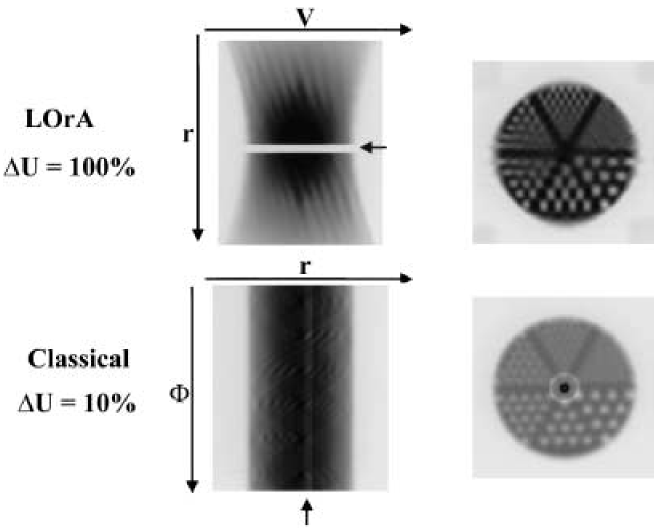

Fig. 8. Comparison between LOrA SPET with a 100% uniformity defect introduced (*small arrow*), and classical SPET with a 10% uniformity defect introduced at the same *r* location (*small arrow*)

fact outside the phantom. The collimator hole length (34 mm) used in LOrA simulations to obtain a similar sensitivity to that achieved by classical SPET was close to the LEHR hole length (40 mm).

When the hole length (*hl*) was fitted to obtain a similar spatial resolution to that of the classical parallel tomography, LOrA SPET achieved an improvement in sensitivity by a factor of about 2.5.

The spatial resolution of LOrA SPET was slightly affected by the gamma detector intrinsic resolution or by the acquisition pixel size: a very high resolution was preserved with an acquisition pixel size of up to 12×12 mm (Fig. 7).

Numerical simulation showed the lack of sensitivity of LOrA SPET to camera uniformity defects (Fig. 8). Even when a 100% uniformity defect was introduced in the acquisition, no artefact was visible in LOrA SPET, whereas even a 10% defect resulted in a significant annular artefact in classical SPET.

The simulation of the cardiac study (Fig. 9) showed a good reconstruction of the heart activity. When only the heart region was scanned, no significant artefact appeared in the heart map.

Phantom acquisitions

The total number of counts in the projections for the 120-min total acquisition time was 146 Mcounts for classical tomography and 128 Mcounts for LOrA, giving a sensitivity ratio of 1.14; this was in good agreement with the figure of 1.09 predicted by the numerical simulation. For both modalities the highest count rate acquisition (960 MBqh) showed slightly worse spatial resolution in the central region of the phantom in comparison with the simulations (Fig. 10). Even using the uniformity correction, classical SPET showed residual circular artefacts in the central region of the phantom. In contrast, without any uniformity correction, LOrA reconstructions were artefact free. For all count rates, LOrA acquisition clearly showed a better spatial resolution than classical SPET: this was especially visible in the fifth sector.

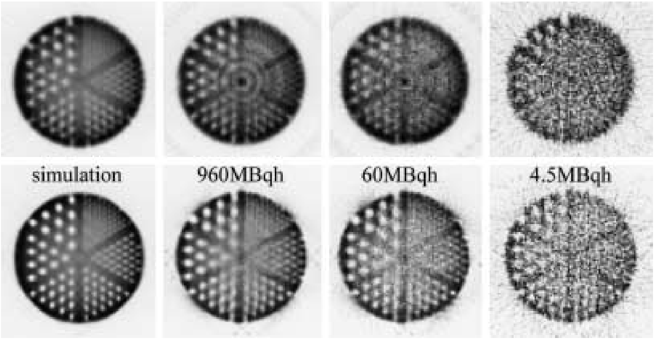

Fig. 10. Comparison between classical SPET (*top row*) and LOrA SPET (*bottom row*) for a noise-free simulation and three different count rates. The sensitivity ratio was 1.14 in favour of classical SPET. The collimator focal length was 13 cm for a transverse collimator FOV of 24 cm. The hole length was 3 cm for both modalities. The hole transverse width was 1.7 mm for classical SPET, and 1.9 mm for LOrA. The hole longitudinal width was 4 mm for both modalities

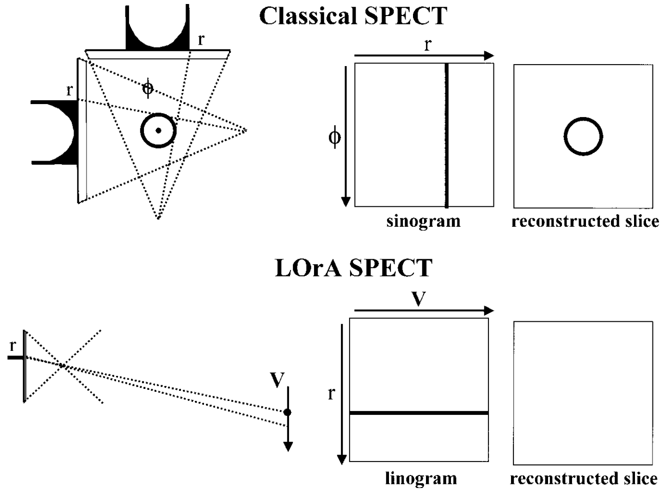

Fig. 11. Sinogram and linogram artefact induced by a localised uniformity defect (*column 2*). Source activity distribution giving acquired sinogram and linogram similar to a uniformity defect (*column 1*). Transverse artefact induced after reconstruction (*column 3*)

Discussion

Uniformity

The surprising very low sensitivity of linogram acquisition in SPET to camera uniformity defects resulted from the permutation of the coordinates along the orbit and the detector between LOrA and classical SPET. Mathematically, in LOrA (or classical) SPET, the reconstruction process corresponds to a ramp filtering on the coordinate V (or r) in the Fourier space followed by an average on the coordinate r (or ϕ). Thus the camera uniformity defects that alter the sinogram and linogram on a specific coordinate r are smoothed in LOrA SPET rather than being magnified, as in classical SPET. Indeed, introducing a linogram with activity independent of the coordinate V in LOrA FBP (Eqs. 2, 3) gives no activity in the reconstructed transverse slice. The intuitive explanation for this benefit is that a uniformity defect always occurs at the same location r in the projections. This corresponds to the acquisition of a source located at an infinite distance from the collimator in LOrA SPET (bottom left, Fig. 11), and thus outside the reconstructed region, rather than to an annular source centred on the rotation axis, as in classical SPET (top left, Fig. 11). The residual ring artefacts in classical SPET acquisition (Fig. 10) were probably due to the different properties of the system for ^{99m}Tc and for ^{57}Co used to construct the uniformity correction table.

Sensitivity and spatial resolution

The absence of Compton scattering in the simulation could explain why, for both modalities, the spatial resolution of the acquisition was slightly worse in the centre of the phantom in comparison with the simulations (Fig. 10).

It is to be noted that, for a source size comparable to the transverse detector FOV, LOrA SPET had a slightly lower sensitivity than classical parallel SPET using a similar collimator hole length and diameter (Figs. 6, 10). Indeed, if some region of the source irradiated the whole detector, typically half of the source was outside the fan-beam collimator acceptance angle (see Appendix B). For this similar sensitivity, the tomographic spatial resolution was much better than with classical SPET. When the hole length was reduced to achieve a tomographic resolution similar to that of classical SPET, a good improvement in sensitivity was obtained. The improvement in sensitivity would be still more pronounced for smaller targets not surrounded by significant activity, as in studies of the brain, thyroid or lumbar spine. In theory, the area containing the whole activity in the slice has to be scanned to avoid truncation artefacts. This could reduce the improvement in sensitivity. Nevertheless, when there was a vertical separation between the target and the activity of no interest, the simulations (Fig. 9) showed that no significant artefact was induced in the scanned area. This was due to the fact that in the linogram from the upper orbit (Fig. 9A), the two activities were well separated. In the left vertical orbit (Fig. 9B) the attenuation reduced the gamma rays emitted from the region farther than the target.

Although it was not possible to find an analytical formula describing the spatial resolution, there were at least three qualitative reasons for this improvement in spatial resolution for similar collimator hole features:

- The location of the target around the focal line, in conjunction with the short focal length of the fan-beam collimator, induced a huge magnification of the target details on the detector area. As a consequence, unlike with classical SPET, the spatial resolution of LOrA SPET is not affected by the limited spatial resolution of the NaI crystal (3.5 mm).

- For similar collimator hole length *l* and diameter *d* the spatial resolution of fan-beam collimator of focal length *f* is improved by a factor $1-l/(2(f+l))$ ([12], p. 413) in comparison with a parallel-hole collimator. For f=12.5 cm and l=4 cm, used in the numerical simulation (Fig. 6), the improvement is about 1.14.
- In comparison with classical SPET, for a similar spatial resolution of the camera (collimator and crystal) in the object plane, the nature of the LOrA SPET process itself reduced the FWHM (or FWTM) in the tomographic slice by a factor of about 1.13 (or 1.30) around the focal line (see Appendix C).

In LOrA SPET the reconstruction of a point source was no longer invariant by rotation, but had a cross shape (see Appendix C). The extension was larger in the direction of the axis bisectrix (x=y and x=–y). As a consequence the FBP reconstruction of two adjacent orbits showed a diagonal tail on the phantom side in opposition to the orbits. Indeed, this was the region where the spatial resolution was worst owing to the longer distance from the collimator. After summation of the reconstruction of the four couples of adjacent orbits, a residual diagonal tail appeared at each diagonal side of the phantom. This artefact was significantly reduced by the attenuation (Fig. 10), the contribution of the gamma rays coming from the farthest region being reduced by their long path through the phantom.

Implementation

In the future development of large FOV solid state detector technology, using classical SPET, all the 3×3 mm crystals (about 20,000) will have their own electronic unit and wiring, greatly increasing the building difficulties. With LOrA SPET it would be possible to use clusters of four 3×3 mm crystals in the transverse direction, reducing the electronic and wiring complexity by a factor of 4 (Fig. 7).

Numerical simulations and acquisitions showed that the theoretical limit that the transverse detector FOV must be at least twice the collimator focal length can in practice be transgressed slightly: the 12.5 cm (or 13 cm) focal length used with the 20 cm (or 24 cm) in the numerical simulations (or acquisition) did not show any visible artefact. Thus, existing small cameras, such as those using solid state detector technology, could directly be used in LOrA SPET. As for classical SPET, rectangular detectors are preferable.

The sensitivity of LOrA SPET was better than that of classical fan-beam tomography, despite using a detector that was half as large and therefore half as expensive

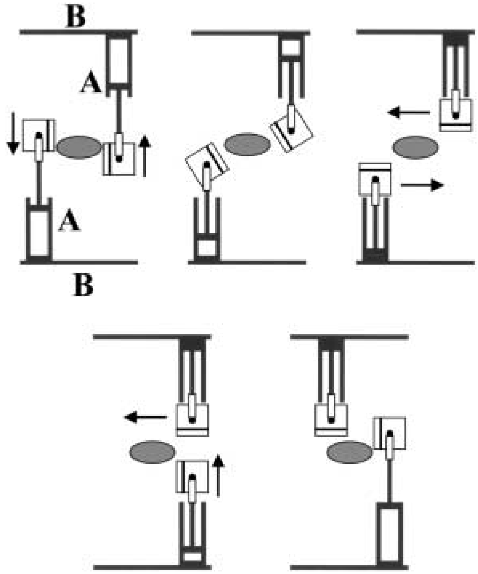

Fig. 12A, B. Two detectors set-up for linogram acquisitions. *Top row:* performance of the four linear orbits in the case of a whole slice study (brain, liver, oncology, bone). *Bottom row:* the two linear orbits needed in cardiac studies. **A** Vertical positioning system. **B** Horizontal positioning system

(Fig. 6). For a similar cost, i.e. using two LOrA detectors, the sensitivity would be improved by a factor of 5. Reducing the detector size will also decrease the weight of the detector shielding; this should facilitate the building of the mechanical parts and thereby help to reduce the cost of the whole system.

An easy way to handle the detector motion along the four linear orbits could be to use two detectors set in opposite positions, each camera being fixed on a vertical linear positioning system, itself carried by a horizontal one (Fig. 12). The camera is fixed inside a fork, allowing rotation around an axis parallel to the length of the patient's body. A major benefit of this configuration is that all weights are well balanced, avoiding use of counterweights and reducing the rigidity needed for the mechanical parts. The top row in Fig. 12 shows how to perform the four linear orbits in the case of a whole slice study (brain, liver, oncology, bone), while the bottom row shows the two linear orbits needed in cardiac studies.

Conclusion

The most obvious benefit of fan-beam LOrA SPET in comparison with fan-beam classical SPET is the absence of truncation artefacts, even when the target is larger than the camera FOV in the transverse plane. This feature could boost the use of expensive solid state technology in SPET by reducing the detector size needed. The truncation problem is one basic reason for the poor success of fan-beam collimator classical SPET in clinical routine. This benefit of LOrA SPET also allows advantage to be taken of the increasing fan-beam collimator tomography sensitivity for decreasing target size, without the need for a collimator with a dedicated focal length, as is the case in classical SPET: only the linear orbit length has to be fitted to the target size. In addition, the optimal orbit can easily, and even automatically, be set up by a fast count rate measurement in relation to the collimator position. A further very surprising benefit is the lack of sensitivity of LOrA SPET to camera uniformity, which is a problem requiring attention in classical SPET, especially when the same camera is used for different energies. These two benefits result from the permutation of the orbit and detector coordinates between LOrA and classical SPET.

The possibility of using a small detector FOV even for a large target size would allow a reduction in the cost of SPET cameras. The very low sensitivity of LOrA SPET to the intrinsic spatial resolution of the detector allows the use of thick NaI crystals for all isotopes, increasing the system sensitivity. Also, thallium-201 cardiac studies will no longer be hampered by the less effective NaI spatial resolution at low energies. Finally, there is the prospect of new gamma detectors with a better energy resolution that are not limited by their spatial resolution features. This should improve the final spatial resolution of the system by decreasing the amount of scattered gamma rays detected.

Nevertheless, the most attractive benefit of LOrA SPET is certainly the improvement in spatial resolution in comparison with parallel or even fan-beam collimator classical SPET, and that for a similar sensitivity. This improvement will be further magnified by the use of a solid state detector, where the final spatial resolution will be less altered by gamma ray scattering in the patient's body.

When the collimator hole length and diameter are fitted in order to obtain a spatial resolution similar to that of classical SPET, an improvement in sensitivity by a factor of about 2.5 is obtained for a 20-cm target size, while using a transverse FOV camera that is half as large. Like classical SPET, LOrA SPET can easily be used with one or two heads in order to further increase the sensitivity; in fact, with LOrA SPET, even four heads may be used. Remember that in classical SPET the number of heads is in practice limited to three as a consequence of orbit geometry management [4].

In the future, accurate simulations (Monte Carlo) taking into account Compton scattering inside the target medium and also inside the collimator will be needed in order to permit correct selection of the collimator characteristics.

Appendix A

Taking the Fourier transform on variable V of Eq. 1, one obtains for the projection P_x (calculus for P_y is similar):

$$p_x(U_x,k,r) = f\int_{-\infty}^{+\infty} dV \int_{-\infty}^{+\infty} d\lambda A \cdot \cdot(-U_x+\lambda f, V-\lambda r)\, e^{-ikV} \tag{A1}$$

Posing $-U_x+\lambda f=x$, $V-\lambda r=y$, the relation is:

$$p_x(U_x,k,r) = \int_{-\infty}^{+\infty} dy \int_{-\infty}^{+\infty} dx A(x,y)\, e^{-iky} e^{-ikxr/f} e^{-ikU_x r/f} \tag{A2}$$

Thus:

$$p_x(U_x,k,r) = a\left(k\frac{r}{f},k\right) e^{-ikU_x\frac{r}{f}}$$

and

$$p_y(U_y,k,r) = a\left(k,k\frac{r}{f}\right) e^{-ikU_y\frac{r}{f}} \tag{A3}$$

Posing $kr/f=k_x$ and $k=k_y$ in the first relation, and $kr/f=k_y$ and $k=k_x$ in the second relation, one obtains:

$$a(k_x,k_y) = e^{ik_xU_x} p_x\left(U_x,k_y,\frac{k_x}{k_y}f\right) = p_x^0\left(k_y,\frac{k_x}{k_y}f\right) \quad \text{if} \quad |k_x|<|k_y| \tag{A4}$$

and:

$$a(k_x,k_y) = e^{ik_yU_y} p_y\left(U_y,k_x,\frac{k_y}{k_x}f\right) = p_y^0\left(k_x,\frac{k_y}{k_x}f\right) \quad \text{if} \quad |k_x|>|k_y| \tag{A5}$$

Thus:

$$\begin{aligned}(2\pi)^2 A(x,y) = & \int_{-\infty}^{0} dk_y \int_{k_y}^{-k_y} dk_x p_x^0\left(k_y,\tfrac{k_x}{k_y}f\right) e^{-ik_xx}e^{-ik_yy} \\ & + \int_{-\infty}^{0} dk_x \int_{k_x}^{-k_x} dk_y p_y^0\left(k_x,\tfrac{k_y}{k_x}f\right) e^{-ik_xx}e^{-ik_yy} \\ & + \int_{0}^{+\infty} dk_y \int_{-k_y}^{k_y} dk_x p_x^0\left(k_y,\tfrac{k_x}{k_y}f\right) e^{-ik_xx}e^{-ik_yy} \\ & + \int_{0}^{+\infty} dk_x \int_{-k_x}^{k_x} dk_y p_y^0\left(k_x,\tfrac{k_y}{k_x}f\right) e^{-ik_xx}e^{-ik_yy}\end{aligned} \tag{A6}$$

Posing $r=f\, k_x/k_y$ and $k=k_y$ in the first and third right members and $r=f\, k_y/k_x$ and $k=k_x$ in the second and fourth ones, one obtains:

$$\begin{aligned}(2\pi)^2 A(x,y) = & \int_{-\infty}^{0} dk \int_{f}^{-f} dr \tfrac{k}{f} p_x^0(k,r)\, e^{-ikxr/f} e^{-iky} \\ & + \int_{-\infty}^{0} dk \int_{f}^{-f} dr \tfrac{k}{f} p_y^0(k,r)\, e^{-ikxr/f} e^{-iky} \\ & + \int_{0}^{+\infty} dk \int_{-f}^{f} dr \tfrac{k}{f} p_x^0(k,r)\, e^{-ikxr/f} e^{-iky} \\ & + \int_{0}^{+\infty} dk \int_{-f}^{f} dr \tfrac{k}{f} p_y^0(k,r)\, e^{-ikxr/f} e^{-iky}\end{aligned} \tag{A7}$$

Permuting the limits $-f$, f in the integration on r in the two first right members and taking into account the fact that k is negative in these two members, one obtains:

$$(2\pi)^2 A(x,y) = \int_{-\infty}^{0} dk \int_{-f}^{f} dr \frac{|k|}{f} p_x^0(k,r)\, e^{-ikxr/f} e^{-iky} + \int_{-\infty}^{0} dk \int_{-f}^{f} dr \frac{|k|}{f} p_y^0(k,r)\, e^{-ikxr/f} e^{-iky} + \int_{0}^{+\infty} dk \int_{-f}^{f} dr |k| f p_x^0(k,r)\, e^{-ikxr/f} e^{-iky} + \int_{0}^{+\infty} dk \int_{-f}^{f} dr \frac{|k|}{f} p_y^0(k,r)\, e^{-ikxr/f} e^{-iky} \quad \text{(A8)}$$

Equation A8 can now be rewritten in the simpler form of Eqs. 2 and 3.

Appendix B

The sensitivity for a fan-beam collimator is ([12] Eqs. 10-14, 10-15, 10-21):

$$\frac{f}{f-b}\frac{d}{l}\alpha \quad \text{(B1)}$$

where f is the focal length, d the hole transverse width, l the hole length, b the distance from the point source to the surface of the collimator and α a normalisation coefficient (the sensitivity in the longitudinal direction is included in α). For $f \to \infty$, Eq. B1 gives the sensitivity of the parallel-hole collimator. For a fan-beam collimator with a FOV twice the focal length, the sensitivity for a square source centred around the focal line (U_x=0 and V=0 in Fig. 3) and with sides of the source parallel to the coordinate axis is:

$$\int_{-L/2}^{+L/2} dy \int_{-y}^{y} dx \frac{f}{y}\frac{d}{l}\alpha = 2fL\frac{d}{l}\alpha \quad \text{(B2)}$$

where L is the size of the square side, f–b=y and the 2D integration is made on the intersection area between the square source and the acceptance triangle of the fan-beam collimator. B2 is the sensitivity for an acquisition at V=0 along the linear orbit. When $|V|$ increases, the sensitivity ratio decreases to 0 when reaching the end of the linear orbit. Assuming a linear decrease (the aim is to estimate the order of magnitude of the sensitivity), the mean sensitivity along the linear orbit is half of Eq. B2.

For a parallel-hole collimator the sensitivity is constant in the source area and also along the revolution orbit, and the mean sensitivity is:

$$\int_{-L/2}^{+L/2} dy \int_{-L/2}^{L/2} dx \frac{d}{l}\alpha = L^2\frac{d}{l}\alpha \quad \text{(B3)}$$

The classical/LOrA SPET sensitivity ratio for the phantom acquisition taking into account the hole diameter of both collimators (fan-beam: d=0.17 cm, parallel-hole: d=0.19 cm) should be about:

$$\frac{L}{f}\frac{0.17}{0.19} = \frac{20}{13}\frac{0.17}{0.19} = 1.38 \quad \text{(B4)}$$

which is not far from the measured factor (1.14). let remember the approximation used in the calculus: square source rather than cylindrical, and linear decreasing versus the linear orbit position.

Appendix C

In order to estimate how the FBP process translates the collimator spatial resolution into the reconstructed plane, we shall consider the simple case of a point source located at the axis origin (x=y=0), with U_α=0 for the LOrA acquisition. The classical SPET rotation radius R is equal to the focal length f of the LOrA fan-beam collimator, so that the distance between the point source and the detector are the same in both modalities. Assume that the system (collimator + detector) spatial resolution is similar for both systems in the vicinity of the axis origin. In this case the point spread function (PSF) of the two systems can be simulated by the Cauchy function [13]:

$$\frac{1}{\pi\sigma}\frac{1}{(1+s^2/\sigma^2)} \quad \text{(C1)}$$

where σ is the collimator spatial resolution and s is the transverse coordinate in the object plane, the FWHM being 2σ. The Cauchy function was preferred to the usual gaussian function as it allowed the possibility of continuing the analytical computation to the end of the FBP reconstruction for both modalities. The LOrA linogram is obtained by replacing s by the orbit coordinate V in C1, while the classical sinogram is obtained by replacing s by the transverse detector coordinate r.

The Fourier transform on the coordinate V for the linogram and on the coordinate r for the sinogram are equal ([14], p. 436):

$$e^{-|k|\sigma} \quad \text{(C2)}$$

For classical SPET the FBP reconstructed activity $A(x, y)$ will be:

$$A(x,y) = \frac{1}{2\pi}\int_0^{2\pi} d\theta \int_0^{\infty} dk\, |k| e^{-|k|\sigma} e^{ikx\cos\theta} e^{iky\sin\theta} \quad \text{(C3)}$$

Using the rotation symmetry of the problem we can limit the study to y=0. C3 can be rewritten as:

$$A(x,0) = \frac{-1}{2\pi}\frac{d}{d\sigma}\int_0^{2\pi} d\theta \int_0^{\infty} dk e^{-|k|\sigma} \cdot \cdot \left(\cos(kx\cos\theta) + i\sin(kx\cos\theta)\right) \quad \text{(C4)}$$

The sine integration vanishes for reasons of parity, and the cosine integration on the spatial frequency k gives ([14], p. 436):

$$A(x,0) = \frac{-1}{2\pi}\frac{d}{d\sigma}\int_0^{2\pi} d\theta \frac{1}{\sigma}\frac{1}{1+x^2\cos^2\theta/\sigma^2} \quad \text{(C5)}$$

The integration on θ is ([14], p. 368, Eq. 375):

$$A(x,0) = \frac{-1}{2\pi}\frac{d}{d\sigma}4\frac{1}{\sigma}\left[\frac{1}{\sqrt{1+x^2/\sigma^2}} tg^{-1}\frac{tg\theta}{\sqrt{1+x^2/\sigma^2}}\right]_0^{\pi/2} \quad \text{(C6)}$$

One obtains:

$$A(x,0) = \frac{-1}{2\pi}\frac{d}{d\sigma}\frac{1}{\sigma}\frac{1}{\sqrt{1+x^2/\sigma^2}} \quad \text{(C7)}$$

Computing the derivative and taking into account the rotation symmetry, the final formula is:

$$A(x,y) = \frac{2}{\sigma^2}\frac{1}{\left(1+(x^2+y^2)/\sigma^2\right)^{3/2}} \quad \text{(C8)}$$

For LOrA SPET, applying the modified FBP algorithm (Eqs. 2, 3) to C2 one obtains:

$$A(x,y) = \frac{1}{(2\pi)^2 f}\int_{-\infty}^{+\infty} dk \int_{-f}^{+f} dr\, |k| e^{-|k|\sigma} \cdot \cdot \left(e^{ik(xr/f+y)} + e^{ik(x+yr/f)}\right) \quad \text{(C9)}$$

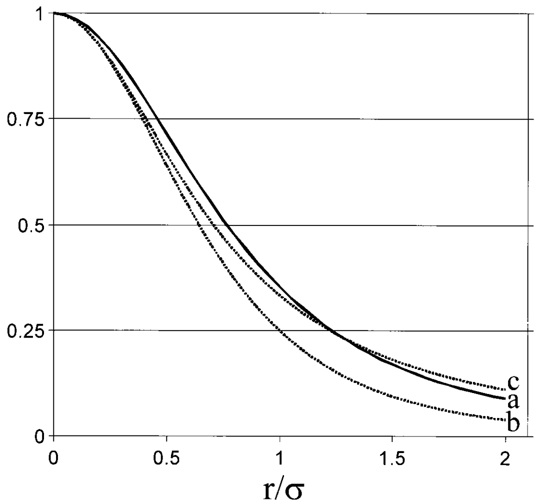

Fig. 13. Normalised profile of the reconstruction of a point source located on the axis origin. *a*, Classical SPET. *b, c* LOrA SPET along the x- or y-axis (*b*) and along the axis bisectrix (*c*). *r* is the distance from the axis origin and, σ is the system spatial resolution

The integration on *r* is immediate and gives:

$$A(x,y)=\frac{1}{(2\pi)^2}\int_{-\infty}^{+\infty}dk\frac{|k|}{k}e^{-|k|\sigma}2\left(\frac{\sin kx}{x}e^{iky}+\frac{\sin ky}{y}e^{ikx}\right) \quad \text{(C10)}$$

Taking into account the parity of cosine and sine, one obtains:

$$A(x,y)=\frac{1}{2\pi}2\int_{0}^{+\infty}dke^{-|k|\sigma}2\left(\frac{\sin kx\cos ky}{x}+\frac{\sin ky\cos kx}{y}\right) \quad \text{(C11)}$$

which can be rewritten as:

$$A(x,y)=\frac{2}{(2\pi)^2}\int_{0}^{+\infty}dke^{-|k|\sigma}\left(\frac{\sin k(x+y)+\sin k(x-y)}{x}+\frac{\sin k(x+y)-\sin k(x-y)}{y}\right) \quad \text{(C12)}$$

The integration on the spatial frequency *k* gives ([14], p. 436):

$$A(x,y)=\frac{1}{(2\pi)^2}\frac{2}{\sigma}\left(\left(\frac{1}{x}+\frac{1}{y}\right)\frac{(x+y)/\sigma}{\left(1+(x+y)^2/\sigma^2\right)}+\left(\frac{1}{x}-\frac{1}{y}\right)\frac{(x-y)/\sigma}{\left(1+(x-y)^2/\sigma^2\right)}\right) \quad \text{(C13)}$$

Reducing to the same denominator, the final formula is obtained:

$$A(x,y)=\frac{2}{\pi^2\sigma}\frac{1}{\left(1+(x+y)^2/\sigma^2\right)}\frac{1}{\left(1+(x-y)^2/\sigma^2\right)} \quad \text{(C14)}$$

Equation C14 shows that in LOrA SPET the reconstructed activity is no longer invariant under rotation, as in classical SPET, but has a cross shape.

From Eqs. C8 and C14 one obtains for the FWHM and FWTM in the reconstructed plane:

$$\text{FWHM\_LOrA}=0.84\ (\text{or } 0.92)\ \text{FWHM\_class if } x=0 \text{ or } y=0\ (\text{or } x=y \text{ or } x=-y) \quad \text{(C18)}$$

$$\text{FWTM}-\text{LOrA}=0.77\ (\text{or } 1.11)\ \text{FWTM}-\text{class if } x=0 \text{ or } y=0\ (\text{or } x=y \text{ or } x=-y) \quad \text{(C19)}$$

Of course, this comparison has some limitations: the PSF function of a camera is not really a Gauchy function, and the computation is performed only when the point source is located on the axis origin (focal line cross point for LOrA or rotation centre for classical SPET). Nevertheless, it shows that the tomographic process itself has an influence on the final spatial resolution in the reconstructed plane (Fig. 13).

References

1. Rosenthal MS, Cullom J, Hawkins W, Moore SC, Tsui BMW, Yester M. Quantitative SPECT imaging: a review and recommendations by the focus committee of the Society of Nuclear Medicine Computer and Instrumentation Council. *J Nucl Med* 1995; 36:1489–1513.
2. Gullberg GT, Zeng GL, Datz FL, Christian PE, Tung CH, Morgan HT. Review of convergent beam tomography in single photon emission computed tomography. *Phys Med Biol* 1992; 37:507–534.
3. Moore SC, Kouris K, Cullum I. Collimator design for single photon emission tomography. *Eur J Nucl Med* 1992; 19: 138–150.
4. Ichihara T. Development of a high-resolution SPECT system. *Toshiba Med Rev* 1990; 33:29–35.
5. van Dulmen A, Walrand S. Method of imaging by SPECT. European Patent Application, publication nr 0898178, 2000; EP1010019.
6. Edholm PR, Herman GT. Linograms in image reconstruction from projections. *IEEE Trans Med Imag* 1987; 6:301–307.
7. Edholm P, Herman GT, Roberts DA. Image reconstruction from linograms: implementation and evaluation. *IEEE Trans Med Imag* 1988; 7:239–246.
8. Anger HO. *Tomographic gamma-ray scanner with simultaneous readout of several planes.* UCRL-16899 REV, Lawrence radiation laboratory. Berkeley: University of California Press, 1966.
9. Chang LT, MacDonald D, Perez-Mendez V. Axial tomography and three dimensional image reconstructive. *IEEE Trans Nucl Sci* 1976; NS-23:568.
10. Hooper HR, Scrimger JW, Lentle BC. Correction for out-of-focal-plane blurring in a simulated multiplane tomographic scanner. *J Nucl Med* 1979; 20:1194–1196.
11. Radon. *Uber die Bestimmung von Funktionen durch ihre Integralwerte langs gewisser Mannigfaltigkeiten.* Akademie der wissenshaften Leipzig, mathematisch physische Klasseberichte 1917; 69:262–277.
12. Rollo DF. *Nuclear medicine physics, instrumentation, and agents.* St. Louis: Mosby, 1977.
13. Soares EJ, Byrne CL, Glick SJ, Appledorn CR, King MA. Implementation and evaluation of an analytical solution to the photon attenuation and non-stationary resolution reconstruction problem in SPECT. *IEEE Trans Nucl Sci* 1993; NS-33: 505–510.
14. Beyer WH. *Standard mathematical tables.* Cleveland: CRC Press, 1976.